

## Volume Changes During Active Shape Fluctuations in Cells

Alessandro Taloni,<sup>1,2</sup> Elena Kardash,<sup>3</sup> Oguz Umut Salman,<sup>1,8</sup> Lev Truskinovsky,<sup>4</sup>  
Stefano Zapperi,<sup>2,1,5,6,\*</sup> and Caterina A. M. La Porta<sup>7,†</sup>

<sup>1</sup>CNR-Consiglio Nazionale delle Ricerche, Istituto per l'Energetica e le Interfasi, Via Roberto Cozzi 53, 20125 Milano, Italy

<sup>2</sup>Center for Complexity and Biosystems and Department of Physics, University of Milano, Via Celoria 16, 20133 Milano, Italy

<sup>3</sup>Departments of Biochemistry and Molecular Biology, Sciences II, 30 Quai Ernest-Ansermet, CH-1211 Geneva 4, Switzerland

<sup>4</sup>LMS, CNRS-UMR 7649, Ecole Polytechnique, Route de Saclay, 91128 Palaiseau, France

<sup>5</sup>Institute for Scientific Interchange Foundation, Via Alassio 11/C, 10126 Torino, Italy

<sup>6</sup>Department of Applied Physics, Aalto University, P.O. Box 14100, FIN-00076 Aalto, Finland

<sup>7</sup>Center for Complexity and Biosystems and Department of Bioscience, University of Milano, Via Celoria 26, 20133 Milano, Italy

<sup>8</sup>CNRS, LSPM UPR3407, Université Paris 13, Sorbonne Paris Cit, 93430 Villetaneuse, France

(Received 3 November 2014; published 19 May 2015)

Cells modify their volume in response to changes in osmotic pressure but it is usually assumed that other active shape variations do not involve significant volume fluctuations. Here we report experiments demonstrating that water transport in and out of the cell is needed for the formation of blebs, commonly observed protrusions in the plasma membrane driven by cortex contraction. We develop and simulate a model of fluid-mediated membrane-cortex deformations and show that a permeable membrane is necessary for bleb formation which is otherwise impaired. Taken together, our experimental and theoretical results emphasize the subtle balance between hydrodynamics and elasticity in actively driven cell morphological changes.

DOI: [10.1103/PhysRevLett.114.208101](https://doi.org/10.1103/PhysRevLett.114.208101)

PACS numbers: 87.17.Aa, 87.16.dm, 87.17.Rt, 87.85.G-

Cells can change their shape to explore their environment, communicate with other cells, and self-propel. These macroscopic changes are driven by the coordinated action of localized motors transforming chemical energy into motion. Active processes in biological systems can be linked to a large variety of collective nonequilibrium phenomena such as phase transitions, unconventional fluctuations, oscillations, and pattern formation [1–3]. A vivid example of actively driven nonequilibrium shape fluctuations is provided by cellular blebs, the rounded membrane protrusions formed by the separation of the plasma membrane from the cortex as a result of actomyosin contraction [4–6].

Blebs occur in various physiological conditions [5,6], as for instance during zebrafish embryogenesis [7–11], or cancer invasion [5]. While some questions have been resolved concerning the mechanisms governing bleb formation and its relation to migration [4–7,12–14], key aspects of bleb mechanics remain unclear. Geometrical constraints dictate that active shape changes associated with blebs should necessarily involve either fluctuations in the membrane surface or in cellular volume, and possibly both. It is generally believed, however, that the cellular volume is not significantly altered during bleb formation, so that the cell is usually considered incompressible [8,12,14]. Yet, experimental evidence *in vitro* suggests that aquaporins (AQPs), a family of transmembrane water channel proteins [15], are involved in cell migration [16–18] and blebbing [19,20]. The implied significance of fluid transport through the membrane suggests that an interplay between hydrodynamic flow and active mechanics has an important but still unclear role in blebbing. In this

Letter, we reveal the role of membrane permeability in the formation, expansion, and retraction of cellular blebs. We show by direct experiments *in vivo* and numerical simulations that bleb formation involves volume fluctuations, considerable water flow through the membrane, and relatively smaller surface fluctuations.

*Experiment.*—One of the limitations impeding the experimental studies of bleb dynamics *in vivo* is the lack of proper tools to generate high-resolution spatial-temporal data. This is due to the fact that the time scale of bleb formation is relatively short (about 1 min, starting from initiation of the bleb to its retraction), which requires fast imaging and photostable markers. Here, we create an improved membrane marker [21] which we inject in one-cell stage zebrafish embryos (see Supplemental Material for experimental methods [22]). Together with wild type (WT) zebrafish primordial germ cells (PGCs), a well-studied biological model to investigate blebbing *in vivo* [7–11], we also consider cells expressing dominant-negative rho kinase mutant (DN-ROK), which inhibits actomyosin contractility suppressing blebbing activity [8]. Zebrafish express a large number of AQPs contributing to the water permeability of the membrane [23]. Here we focus on AQP1 and AQP3, the most ubiquitously expressed aquaporins [22,23]. To assess their role in volume change and blebbing, we consider PGCs with AQP1 and AQP3 overexpression (AQP+) and knockdown (AQP–).

The imaging of blebbing is done during 12–16 h postfertilization, when we record a time series of confocal images for a large number of cells. Sequences of image stacks are then processed using the 3D Active Meshes algorithm implemented in the ICY software [24].

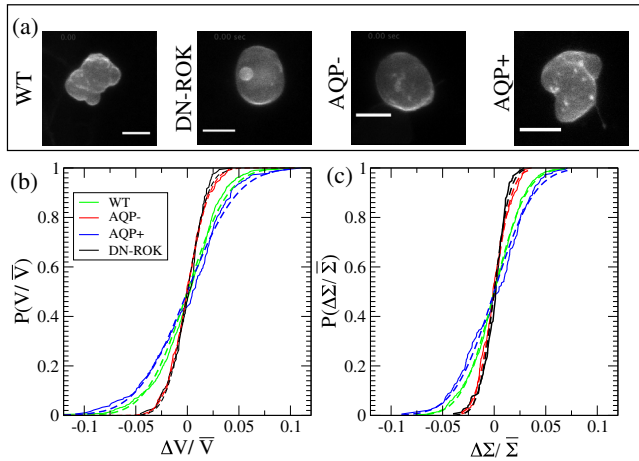


FIG. 1 (color online). Volume and surface fluctuations during blebbing are controlled by AQPs. (a) Representative phenotypes for bleb formation in PGCs under different conditions: wild type (WT), cells expressing DN-ROK mutant which impairs contractility by interfering with actomyosin contraction (DN-ROK), cells where AQP1a and AQP3a are suppressed (AQP<sup>-</sup>), cells with overexpression of AQP1a and AQP3a (AQP<sup>+</sup>). The scale bar corresponds to 10  $\mu\text{m}$ . The cumulative distribution of relative volume (b) and surface (c) fluctuations for the four conditions illustrated in (a), together with a Gaussian fit (dashed lines). The distributions are sampled over  $N$  different time frames corresponding to  $n$  different cells. (WT:  $n = 15$  cells and  $N = 800$  time-frames; DN-ROK:  $n = 2$  and  $N = 155$ ; AQP<sup>-</sup>:  $n = 4$  and  $N = 180$ ; and AQP<sup>+</sup>:  $n = 7$  and  $N = 183$ .)

The algorithm performs three-dimensional segmentation and tracking using a triangular mesh that is optimized using the original signal as a target. From the resulting three-dimensional mesh, one can then measure the cell volume and its surface area (see also the Supplemental Material [22]). In Fig. 1(a), we illustrate representative phenotypes of PGCs under different conditions (see movies in the Supplemental Material [22]). These observations show that WT cells display a marked blebbing activity that, as expected, is strongly suppressed when active contraction is hindered, as in DN-ROK cells [8]. Remarkably, we also observe a strong reduction in bleb activity in AQP<sup>-</sup> cells, where water flow is hindered. In contrast, water flow enhances blebbing as manifested by the presence of larger blebs in the AQP<sup>+</sup> condition. To quantify these qualitative observations, we measure the cell volume  $V$  and its surface  $\Sigma$ , sampling the results over a large number of time frames taken on different cells. To account for cell-to-cell variability, we consider relative volume  $\Delta V/\bar{V} = (V - \bar{V})/\bar{V}$  and surface  $\Delta\Sigma/\bar{\Sigma} \equiv (\Sigma - \bar{\Sigma})/\bar{\Sigma}$  changes, where  $\bar{V}$  ( $\bar{\Sigma}$ ) is the time-averaged volume (surface) of each cell. The average value of the volume  $V$  does not change significantly for the four cases (see the Supplemental Material [22]).

In Fig. 1(b) we show the cumulative distribution of relative volume changes which indicates significant fluctuations, reaching up to 10%, in the WT case. Volume fluctuations are strongly reduced for the DN-ROK and

AQP<sup>-</sup> cases, while they are enhanced in the AQP<sup>+</sup> case. The relative volume and surface distributions themselves are well described by Gaussian statistics, as also confirmed by a Kolmogorov-Smirnov test (see the Supplemental Material [22]). A statistical test also indicates that the differences between WT and both AQP<sup>-</sup> and DN-ROK are significant ( $p < 0.01$ ), but the differences between WT and AQP<sup>+</sup> and between AQP<sup>-</sup> and DN-ROK are not [22]. Relative surface fluctuations are smaller than volume fluctuations in the WT case and are further reduced for DN-ROK and AQP<sup>-</sup> and slightly increased for AQP<sup>+</sup> [see Fig. 1(c)]. We also checked that relative surface and volume fluctuations are correlated [22], suggesting a direct link between blebbing activity and volume fluctuations induced by water transport. Suppressing water flow has the same effect as suppressing active contraction; in both cases, blebs are hindered. Furthermore, the volume fluctuations we observe follow closely the bleb expansion and retraction as illustrated in Fig. 2. Expansion of a bleb corresponds to a visible volume increase while, when a bleb retracts, the volume decreases. Here, we concentrate on AQP<sup>+</sup> PGC since the blebs are distinctly visible and the analysis clearer, but the same result holds for WT cells where, however, several blebs may form and retract simultaneously.

*Model.*—In order to better understand the physical role of water flow in bleb formation, we resort to numerical simulations of a two-dimensional model of the biomechanics of cortex-membrane deformations, including fluid transport through the plasma membrane. Several existing computational models for cellular blebs

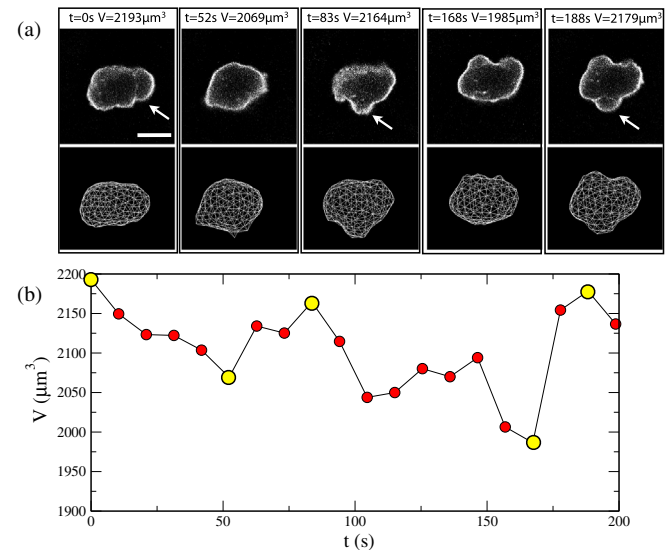


FIG. 2 (color online). Bleb formation is directly related to volume changes. (a) Time lapse of a single AQP<sup>+</sup> cell. Two-dimensional sections are shown in the upper panels and the corresponding reconstructed three-dimensional meshes in the lower ones. Arrows indicate blebs. The scale bar corresponds to 1  $\mu\text{m}$ . (b) Evolution of the volume for the same cell. Time points corresponding to the panels in (a) are denoted in yellow. An increase in volume is observed in correspondence with each newly formed bleb.

simulate the detachment and expansion of the membrane due to the active contraction of the cortex, assuming cell volume conservation [25–28]. Here, we relax this assumption by introducing and varying the membrane permeability  $\alpha$  [29] in a model based on the immersed boundary method [30] in the Stokes approximation [31], considering a contracting discretized elastic cortex coupled to an elastic membrane.

We describe both the membrane and the cortex by a set of discrete nodes connected by springs on one-dimensional closed curves parametrized by their initial arc length  $s$  with  $s \in [0, 2\pi]$ . Using Lagrangian coordinates, the position of node  $i$  is denoted by  $\mathbf{r}_{m_i}(t)$  (for the membrane) and  $\mathbf{r}_{c_i}(t)$  (for the cortex). Initial positions are chosen to be  $\mathbf{r}_{m_i} = (r_m \cos(s), r_m \sin(s))$  and  $\mathbf{r}_{c_i} = (r_c \cos(s), r_c \sin(s))$ , where  $r_m$  and  $r_c$  are the membrane and cortex radii, respectively. The interactions between the nodes on their respective curves include nearest-neighbor (NN) and three-body interaction terms to account for stretching and bending energies. We also model the cortex-membrane interface by a set of springs with random stiffness  $k_{mc}$  ( $\text{N m}^{-3}$ ), drawn from a uniform distribution. Disorder in the stiffness represents at a coarse-grained scale the random arrangement of cortex-membrane linker proteins. The energy of the system can be decomposed as  $\mathcal{E} = \mathcal{E}_c + \mathcal{E}_m + \mathcal{E}_{\text{int}}$ . The first two terms are given by

$$\mathcal{E}_x = \epsilon_x \sum_{i=1}^N \left[ \frac{k_x}{2} \left( \frac{|\mathbf{r}_{x_{i+1,i}}| - \epsilon_x}{\epsilon_x} \right)^2 + \frac{B_x}{2\epsilon_x^2} (\cos(\theta_{x_{i-1,i,i+1}}) - \cos(\theta_{x_{i-1,i,i+1}}^0))^2 \right], \quad (1)$$

where  $x$  corresponds to either membrane ( $m$ ) or cortex ( $c$ ),  $|\mathbf{r}_{x_{i+1,i}}|$  is the distance between node  $i$  and  $i+1$ ,  $\epsilon_x$  is the equilibrium distance between NN nodes,  $k_x$  ( $\text{N/m}$ ) is the stiffness coefficient,  $B_x$  ( $\text{J}$ ) is the bending coefficient,  $\theta_{i-1,i,i+1}$  and  $\theta_{i-1,i,i+1}^0$  are the angles between the triplets  $(i-1, i, i+1)$  in deformed and equilibrium configurations, respectively. The interaction energy is given by  $\mathcal{E}_{\text{int}} = \sum_i k_{mc} (|\mathbf{r}_{mc_i}| - l)^2/2$ , where  $|\mathbf{r}_{mc_i}|$  and  $l$  are the distances between the membrane and cortex node with the same index  $i$  in the deformed and equilibrium configurations. A nonvanishing rest length  $\epsilon_c$  for the cortex element is needed to prevent the cortex from collapsing under hydrostatic forces and represents a convenient method [32–34] to account for osmotic regulation present in cells [35]. Cortex elements are assumed to follow overdamped dynamics  $\mu_c \dot{\mathbf{r}}_{c_i} = -\delta\mathcal{E}/\delta\mathbf{r}_{c_i}$ , where  $\mu_c$  ( $\text{kg m}^{-2} \text{s}^{-1}$ ) is the cortical drag coefficient.

We first consider an impermeable elastic membrane that moves with the fluid velocity satisfying a no-slip boundary condition. The fluid velocity  $\mathbf{u}$  and the pressure  $p$  satisfy the Stokes equation with the incompressibility constraint,

$$\mu \Delta \mathbf{u} = \nabla p - \mathbf{f}, \quad \nabla \cdot \mathbf{u} = 0, \quad (2)$$

where  $\mu$  is the fluid viscosity and  $\mathbf{f}$  is the body force per unit volume ( $\text{N m}^{-3}$ ) that can be calculated by spreading the force density  $\mathbf{F}_{m_i}$  from solid (Lagrangian  $\mathbf{r}_{m_k}$ ) to fluid (Euler  $\mathbf{r}$ ) coordinates as  $\mathbf{f}(\mathbf{r}) = \sum_{k=1}^N \mathbf{F}_{m_k} \delta_h(\mathbf{r} - \mathbf{r}_{m_k})$ , where  $\mathbf{F}_{m_k} = -\delta\mathcal{E}/\delta\mathbf{r}_{m_k}$  and  $\delta_h(\mathbf{r})$  is the two-dimensional discretized delta function. Equation (2) is solved using the regularized Stokeslet method [31] as in Ref. [27]. After the velocity has been calculated in Euler coordinates, we evolve the membrane nodes as  $\dot{\mathbf{r}}_{m_k} = \mathbf{u}(\mathbf{r}_{m_k})$ . We take special care to correct  $\mathbf{u}(\mathbf{r}_{m_k})$  to enforce volume conservation, a common problem of the immersed boundary method [22,29,36].

Cortex contraction and healing are the main driving forces of the blebbing activity. In our model, we assume that the cortex is prestretched, an assumption which we impose by choosing a value for the equilibrium distance between the nodes  $\epsilon_c$  that is smaller than their initial distances. Bleb nucleation in our model occurs stochastically due to the randomness of the stiffness of the bonds representing the membrane-cortex interface. Local detachment is then implemented by setting to zero the bond stiffness  $k_{mc}$  if its stretching  $|\mathbf{r}_{mc_i}|$  is above a threshold that we set at  $0.1l$ . Finally, to implement interface healing, we assume that each cortex node  $i$ , associated with a removed interface bond, moves toward the membrane with velocity  $\mathbf{v} = \nu_c \mathbf{r}_{mc_i}/|\mathbf{r}_{mc_i}|$  until it attaches again when  $|\mathbf{r}_{mc_i}| \leq l$  [27]. When disconnected nodes become connected again, we assign new random values to the stiffness  $k_{mc}$  of the bond. We observe that the strength of disorder (i.e., the wideness of its distribution) controls bleb nucleation, which in turn may cause the presence of a large number of blebs, occurring simultaneously. As in previous models [25–28], we neglect additional time-dependent effects due to viscoelasticity and actin turnover in the cortex [37].

We introduce permeability into the model by following Ref. [29]. We assume Darcy's law and impose a porous slip velocity normal to the membrane given by

$$u_p(\mathbf{r}_{m_k}) = -\frac{K}{\mu} \frac{\partial P}{\partial n} \approx -\frac{K}{\mu} \frac{[P]}{a}, \quad (3)$$

where  $K$  is permeability,  $\mu$  is the viscosity,  $a$  is membrane thickness, and  $[P]$  is the pressure jump. Using the normal stress jump condition  $[P] = \mathbf{F} \cdot \mathbf{n}/\Delta S(\mathbf{r}_{m_k})$ , the porous velocity  $u_p$  reads  $u_p(\mathbf{r}_{m_k}) = -\alpha \mathbf{F} \cdot \mathbf{n}/\Delta S(\mathbf{r}_{m_k})$ , where  $\alpha = K/(\mu a)$  ( $\text{m}^2 \text{s}/\text{kg}$ ) and  $\mathbf{F}$  is the force on the node. Finally, we reach the equation used in the simulations  $\dot{\mathbf{r}}_{m_k} = \mathbf{u}^{\text{corr}}(\mathbf{r}_{m_k}) + u_p(\mathbf{r}_{m_k})$ .

*Simulations.*—To simulate the model, we assume a square fluid domain that we discretize using a square grid with a discretization step  $dx = L/N_E$  and  $dy = L/N_E$ , where  $L$  is the length of the domain in each direction and  $N_E \times N_E$  is the number of Eulerian coordinates. The fluid domain covers both the inside and outside of the membrane and has an area of  $100 \times 100 \mu\text{m}$ . The discretization steps  $dx$  and  $dy$  are of size  $1 \mu\text{m}$ .

The membrane permeability in zebrafish embryos has been measured experimentally and is reported to be in the range  $3 \times 10^{-15} < \alpha < 2 \times 10^{-14} \text{ m}^2 \text{ s/kg}$ , depending on the developmental stage [38]. Here, we perform numerical simulations under different values of  $\alpha$ , ranging from  $\alpha = 0$  to  $\alpha = 8 \times 10^{-14} \text{ m}^2 \text{ s/kg}$ , to account for AQP overexpression and knockdown (see Table S1 in the Supplemental Material for a complete list of parameters). When  $\alpha$  is in the physiological range, we observe realistic bleb formation and retraction (Fig. 3(a) and movie S5 [22]). When we delete membrane permeability, setting  $\alpha = 0$  and enforcing strict cell volume conservation, bleb activity is suppressed [Fig. 3(b) and movie S6 [22]]. We can relate the simulations to the experimental results by noticing that the cell area  $A$ , the two-dimensional analogue of the three-dimensional cell volume  $V$ , fluctuates more or less when the permeability is increased or reduced [see Figs. 3(c) and 3(d)], in correspondence with AQPs overexpression or knockdown, respectively [23]. Both experiments and simulations suggest that blebs occur as long as the fluid is able to flow sufficiently fast through the membrane.

*Discussion.*—Our model allows us to better understand why volume fluctuations are crucial for blebbing. Actomyosin-driven cortex contraction leads to a shrinkage of the cell by squeezing some water outside. Indeed, the fluid pressure inside the cell is initially larger than the one outside [see Fig. 3(a)]. The contraction of the cortex induces stretching in the membrane-cortex linkers, leading the membrane to buckle [39]. Buckling provides an

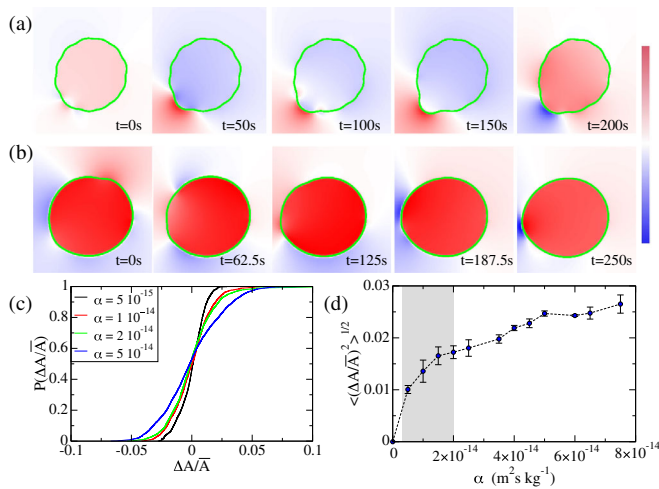


FIG. 3 (color online). Numerical simulations show that membrane porosity is needed for blebbing. (a) A series of snapshots of the numerical simulations of bleb formation and retraction. The color represents the local fluid pressure, red for positive and blue for negative pressures while the cell membrane is green. (a) Results obtained with physiological permeability:  $\alpha = 2 \times 10^{-14} \text{ m}^2 \text{ s/kg}$ . (b) For  $\alpha = 0$ , bleb formation is impaired. (c) The cumulative distribution of relative area fluctuations for different permeabilities. (d) The standard deviation of the distribution of relative cell areas as a function of permeability. The physiological range is depicted in gray.

effective way for membranes to avoid considerable elastic compression and is associated with a structural softening of the system [40,41]. Furthermore, it allows us to generate large membrane deflections needed to form a bleb. In differentiated cells, additional membrane surface can be obtained by disassembling caveolae [42], but this cannot happen in PGCs where caveolin is not expressed. When the interface fractures, the mechanical stress on the detached part of the membrane decreases, but it increases on the interface that is still attached, inducing crack propagation. As the bleb expands, the fluid pressure inside the cell is reduced [see Fig. 3(a)] leading to an inflow of water. In Fig. 4(a), we display the spatiotemporal evolution of the pressure jump across the membrane, showing large fluctuations in correspondence to bleb formation (see the Supplemental Material [22]). These pressure spikes, whose distribution is long-tailed [Fig. 4(b)], are a manifestation of the stress concentrations around cracks and are needed to account for the observed volume fluctuations; otherwise, the average pressure jump generated by a uniform cortex contraction (around  $10^2 \text{ Pa}$ ) would not displace a sufficient amount of fluid during the short lifetime of a bleb [14,35]. Healing of the membrane-cortex interface eventually leads to bleb retraction and to increased fluid pressure inside the cell. The mechanism described above does not work for an impermeable membrane: isochoric buckling is possible in principle but, in addition to bending, it necessarily causes considerable stretching which is energetically expensive [39]. Thus, when the interface fractures, the bleb does not form and interface delamination takes place without localized membrane expansion.

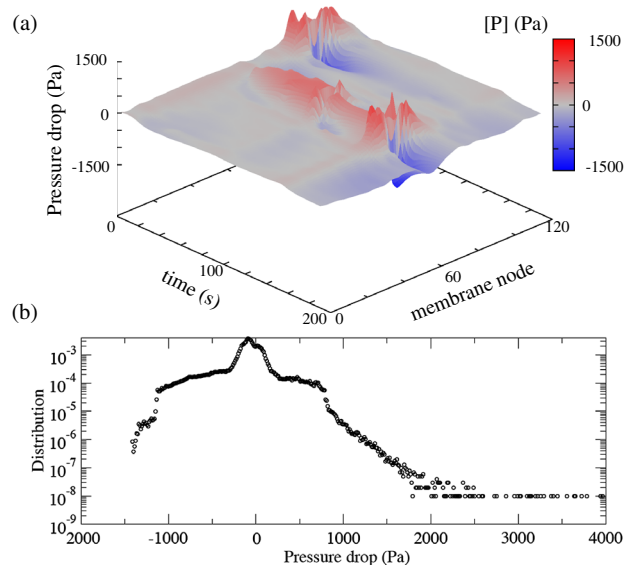


FIG. 4 (color online). (a) Spatio-temporal evolution of the pressure jump across the membrane computed from the normal stress jump condition in numerical simulations with  $\alpha = 2 \times 10^{-14} \text{ m}^2 \text{ s/kg}$ . The pressure drop is strongly enhanced in localized regions corresponding to blebs. (b) The corresponding distribution of pressure jumps displays long tails.

Our numerical results show that volume fluctuations during blebbing are due to mechanically induced highly nonuniform pressure drops across the membrane. The same mechanism could also explain the experimental observation that blebs are nucleated preferentially in regions of negative membrane curvature [43]. Changes in osmotic pressure gradients could also contribute to the process, as suggested previously [13,20,44], but are not explicitly included in our model. Future experimental work will clarify if this and other assumptions present in our model are correct, but our results should stimulate both new experiments and the development of more elaborate theories and models. This work would also allow us to better understand the role of transmembrane water transport for other cellular protrusions, given that past experimental results relate the presence of aquaporins to the formation of lamellipodia [17] and filopodia [20]. The present methodology provides the basis for a physical explanation of this broad class of phenomena.

We thank A. Dufour, A. L. Sellerio, and D. Vilone for useful discussions. A. T., O. U. S., and S. Z. are supported by the European Research Council through the Advanced Grant No. 291002 SIZEEFFECTS. S. Z. acknowledges support from the Academy of Finland FiDiPro program, Project No. 13282993. C. A. M. L. P. acknowledges financial support from MIUR through PRIN 2010. E. K. acknowledges the support of a FEBS long-term postdoctoral fellowship while writing this manuscript.

A. Taloni, E. Kardash, and O. U. Salman contributed equally to this Letter.

---

\*stefano.zapperi@unimi.it

†caterina.laporta@unimi.it

- [1] M. C. Marchetti, J. F. Joanny, S. Ramaswamy, T. B. Liverpool, J. Prost, M. Rao, and R. A. Simha, *Rev. Mod. Phys.* **85**, 1143 (2013).
- [2] S. Ramaswamy, *Annu. Rev. Condens. Matter Phys.* **1**, 323 (2010).
- [3] J. B. Manneville, P. Bassereau, S. Ramaswamy, and J. Prost, *Phys. Rev. E* **64**, 021908 (2001).
- [4] G. Charras and E. Paluch, *Nat. Rev. Mol. Cell Biol.* **9**, 730 (2008).
- [5] O. T. Fackler and R. Grosse, *J. Cell Biol.* **181**, 879 (2008).
- [6] E. K. Paluch and E. Raz, *Curr. Opin. Cell Biol.* **25**, 582 (2013).
- [7] E. Kardash, M. Reichman-Fried, J.-L. Maître, B. Boldajipour, E. Papusheva, E.-M. Messerschmidt, C.-P. Heisenberg, and E. Raz, *Nat. Cell Biol.* **12**, 47 (2010).
- [8] H. Blaser, M. Reichman-Fried, I. Castanon, K. Dumstrei, F. L. Marlow, K. Kawakami, L. Solnica-Krezel, C.-P. Heisenberg, and E. Raz, *Dev. Cell* **11**, 613 (2006).
- [9] E. Raz, *Nat. Rev. Genet.* **4**, 690 (2003).
- [10] B. E. Richardson and R. Lehmann, *Nat. Rev. Mol. Cell Biol.* **11**, 37 (2010).
- [11] K. Tarbashevich and E. Raz, *Curr. Opin. Cell Biol.* **22**, 715 (2010).
- [12] G. T. Charras, J. C. Yarrow, M. A. Horton, L. Mahadevan, and T. J. Mitchison, *Nature (London)* **435**, 365 (2005).
- [13] G. T. Charras, M. Coughlin, T. J. Mitchison, and L. Mahadevan, *Biophys. J.* **94**, 1836 (2008).
- [14] J.-Y. Tinevez, U. Schulze, G. Salbreux, J. Roensch, J.-F. Joanny, and E. Paluch, *Proc. Natl. Acad. Sci. U.S.A.* **106**, 18581 (2009).
- [15] L. S. King and P. Agre, *Annu. Rev. Physiol.* **58**, 619 (1996).
- [16] A. S. Verkman, *J. Cell Sci.* **118**, 3225 (2005).
- [17] E. Monzani, R. Bazzotti, C. Perego, and C. A. M. La Porta, *PLoS One* **4**, e6167 (2009).
- [18] K. M. Stroka, H. Jiang, S.-H. Chen, Z. Tong, D. Wirtz, S. X. Sun, and K. Konstantopoulos, *Cell* **157**, 611 (2014).
- [19] R. C. Huebert, M. M. Vasdev, U. Shergill, A. Das, B. Q. Huang, M. R. Charlton, N. F. LaRusso, and V. H. Shah, *Hepatology* **52**, 238 (2010).
- [20] T. Karlsson, A. Bolshakova, M. A. O. Magalhães, V. M. Loitto, and K.-E. Magnusson, *PLoS One* **8**, e59901 (2013).
- [21] A. W. Nguyen and P. S. Daugherty, *Nat. Biotechnol.* **23**, 355 (2005).
- [22] See Supplemental Material at <http://link.aps.org/supplemental/10.1103/PhysRevLett.114.208101> for detailed experimental methods, image processing methodology, supplemental figures with experimental and numerical data, animations of experiments, and simulations.
- [23] A. Tingaud-Sequeira, M. Calusinska, R. N. Finn, F. Chauvigné, J. Lozano, and J. Cerdà, *BMC Evol. Biol.* **10**, 38 (2010).
- [24] A. Dufour, R. Thibeaux, E. Labruyère, N. Guillén, and J.-C. Olivo-Marin, *IEEE Trans. Image Process.* **20**, 1925 (2011).
- [25] J. Young and S. Mitran, *J. Biomech.* **43**, 210 (2010).
- [26] F. Y. Lim, K.-H. Chiam, and L. Mahadevan, *Europhys. Lett.* **100**, 28004 (2012).
- [27] F. Y. Lim, Y. L. Koon, and K.-H. Chiam, *Comput. Meth. Biomech. Biomed. Eng.* **16**, 1085 (2013).
- [28] W. Strychalski and R. D. Guy, *Math. Med. Biol.* **30**, 115 (2013).
- [29] J. M. Stockie, *Comput. Struct.* **87**, 701 (2009).
- [30] C. S. Peskin, *Acta Numer.* **11**, 479 (2002).
- [31] R. Cortez, *SIAM J. Sci. Comput.* **23**, 1204 (2001).
- [32] E. L. Barnhart, G. M. Allen, F. Jülicher, and J. A. Theriot, *Biophys. J.* **98**, 933 (2010).
- [33] X. Du, K. Doubrovinski, and M. Osterfield, *Biophys. J.* **102**, 1738 (2012).
- [34] P. Recho, T. Putelat, and L. Truskinovsky, *Phys. Rev. Lett.* **111**, 108102 (2013).
- [35] H. Jiang and S. X. Sun, *Biophys. J.* **105**, 609 (2013).
- [36] E. P. Newren, Ph. D. thesis, University of Utah, 2007.
- [37] M. Fritzsche, A. Lewalle, T. Duke, K. Kruse, and G. Charras, *Mol. Biol. Cell* **24**, 757 (2013).
- [38] M. Hagedorn, F. W. Kleinhans, R. Freitas, J. Liu, E. W. Hsu, D. E. Wildt, and W. F. Rall, *J. Exp. Zool.* **278**, 356 (1997).
- [39] E. Katifori, S. Alben, and D. R. Nelson, *Phys. Rev. E* **79**, 056604 (2009).
- [40] J. Kierfeld, P. Gutjahr, T. Kühne, P. Kraikivski, and R. Lipowsky, *J. Comput. Theor. Nanosci.* **3**, 898 (2006).
- [41] P. Sens and N. Gov, *Phys. Rev. Lett.* **98**, 018102 (2007).
- [42] B. Sinha *et al.*, *Cell* **144**, 402 (2011).
- [43] R. A. Tyson, E. Zatulovskiy, R. R. Kay, and T. Bretschneider, *Proc. Natl. Acad. Sci. U.S.A.* **111**, 11703 (2014).
- [44] J. You, S. Aznavoorian, L. A. Liotta, and C. Dong, *J. Cell Physiol.* **167**, 156 (1996).